

# Coupling between waveguides and microresonators: the local approach

DASHIELL L. P. VITULLO<sup>1\*</sup>, SAJID ZAKI<sup>3</sup>, D. E. JONES<sup>1</sup>, M. SUMETSKY<sup>3</sup>, AND MICHAEL BRODSKY<sup>1,2</sup>

<sup>1</sup>U.S. Army Research Laboratory, Adelphi, MD 20783-1193, USA

<sup>2</sup>U.S. Military Academy, West Point, NY 10996, USA

<sup>3</sup>Aston Institute of Photonic Technologies, Aston University, Birmingham B4 7ET, UK

\*Corresponding author: [Dashiell.L.Vitullo.civ@mail.mil](mailto:Dashiell.L.Vitullo.civ@mail.mil)

Coupling between optical microresonators and waveguides is a critical characteristic of resonant photonic devices with complex behavior that is not well understood. However, if the characteristic variation length of the microresonator modes is much larger than the waveguide width, the coupling parameter behavior is simplified. This condition is satisfied for whispering gallery modes in an elongated bottle microresonator with nanoscale effective radius variation, when coupled to a microfiber waveguide. Here, we use such a microresonator to experimentally investigate the local coupling parameters, which are independent of the mode distribution, and establish the values and interdependencies between these coupling parameters.

Photonic devices based on optical microresonators commonly include waveguides, which are used to couple light in and out of microresonators. The performance of these devices is determined by the optical characteristics of microresonators and waveguides as well as by the coupling between them. The theoretical and experimental investigation of microresonators with different shapes (rings, spheres, toroids, bottles, etc.) is of great current interest and has been intensively developed for different applications [1-3]. Less attention was given to the investigation of dependencies of coupling parameters on the optical and geometric characteristics of waveguides and microresonators [4-10]. These dependencies are quite complex [4,5] and in many cases it is easier to determine them experimentally [6-11]. However, understanding the basic features of coupling between waveguides and microresonators, especially of those with three-dimensional geometry (e.g., microspheres and microbottles), is important for the future development of resonant microdevices for classical [4,5,8-11] and quantum [6,7,12-14] applications. One approximation used

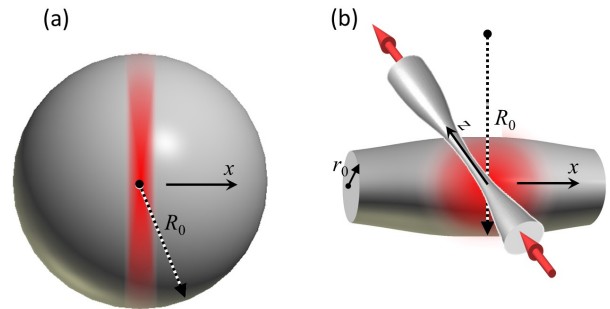


**Fig. 1.** (a) WGM in a microsphere resonator. (b) WGM in a bottle microresonator.  $R_0$  and  $r_0$  are the axial and radial radii of curvature, respectively.

in the calculation of coupling parameters is based on relatively small dimensions of the region where waveguide and resonator modes interact. This permits simplification of the overlap integrals determining the coupling parameters [15]. Here we go further and show that this approximation allows us to significantly advance our understanding of the microresonator-waveguide coupling by revealing relationships between field-independent coupling parameters.

First, we illustrate our idea with the example of a waveguide coupling to the whispering gallery modes (WGMs) of a spherical microresonator, shown in Fig. 1(a). In the cylindrical coordinate system  $(x, r, \phi)$ , the fundamental WGM at the surface of a sphere of radius  $R_0$  behaves as  $\exp(im\phi) \exp(-mx^2/R_0^2)$  [4] where the azimuthal quantum number can be expressed though the WGM resonant wavelength  $\lambda_{\text{res}}$  and effective refractive index  $n_e$  as  $m \approx 2\pi n_e R_0 / \lambda_{\text{res}}$ . The degeneracy of this mode is lifted by the

asymmetry of the sphere, which is unavoidable in practice [6]. The characteristic variation length of this mode along axis  $x$  is  $x_c = (\lambda R_0/2\pi n_e)^{1/2}$ . Setting  $R_0 = 100 \mu\text{m}$ ,  $\lambda_{\text{res}} = 1.5 \mu\text{m}$ , and  $n_e = 1.5$ , we have  $x_c = 4 \mu\text{m}$ , while for a larger  $R_0 = 1 \text{mm}$ , we have  $x_c = 12 \mu\text{m}$ . It is instructive to compare these characteristic lengths to those of the coupling waveguides. Possible types of waveguides used for coupling to microresonators include optical microfibers [16] and planar waveguides [17]. For the optimal width of these waveguides [16], their characteristic coupling region coincides with their width  $w$ . Then, provided that  $w \ll x_c$ , the waveguide-microresonator coupling will be determined by the local value of the WGM field at the waveguide position. For a silica microfiber  $w \sim 1 \mu\text{m}$  [15], while for a silicon waveguide  $w \sim 0.3 \mu\text{m}$  [17]. Thus, for a relatively large radius  $R_0$ , the condition of local coupling  $w \ll x_c$  is satisfied.

A much larger ratio of  $x_c/w$  can be achieved with an elongated bottle microresonator [Fig. 1(b)]. The fundamental WGM in this resonator behaves as  $\exp(im\phi) \exp(-x^2/x_c^2)$  with  $x_c = (2R_0r_0)^{1/4} \lambda_{\text{res}}^{1/2} (2\pi n_e)^{-1/2}$  where  $R_0$  and  $r_0$  are the axial and radial radii of the resonator shown in Fig. 1(b) [18]. As an example, for  $R_0 = 30 \text{m}$  and  $r_0 = 19 \mu\text{m}$  taken from our experiment described below, we have  $x_c = 75 \mu\text{m}$  which is significantly greater than the diameter of microfiber  $w \sim 1 \mu\text{m}$  used in our experiment.

The waveguide in our experimental system is a micrometer diameter waist (microfiber) of a biconical optical taper shown in Fig. 1(b). We change the coupling by moving one of the devices relative to the other, thus varying the position where the microfiber and bottle microresonator make contact. The coupling depends on the local diameter of the taper at the contact point along its longitudinal axis  $z$ , as well as the position along the resonator's longitudinal axis  $x$  where the microfiber makes contact. The bottle microresonator considered in our experiment has very small nanoscale effective radius variation  $\Delta r_{\text{eff}}(x)$ ; therefore, the resonant transmission power through the microfiber [15] is described by

$$P(\lambda, x, z) = \left| S_0(z) - \frac{i |C(z)|^2 G(\lambda, x, x)}{1 + D(z)G(\lambda, x, x)} \right|^2, \quad (1)$$

where  $\lambda$  is the vacuum wavelength. Here  $S_0(z)$  is the nonresonant transmission amplitude and  $C(z)$  and  $D(z)$  are called the *local coupling parameters* as they don't depend on the cavity mode.  $G(\lambda, x, x)$  is the Green's function of the one-dimensional wave equation describing the propagation of WGMs along the bottle axis  $x$ :

$$\frac{\partial^2 \Psi}{\partial x^2} + \beta^2(\lambda, x) \Psi = 0. \quad (2)$$

Here  $\beta(\lambda, x) = 2^{1/2} \beta_0 [(\Delta r_{\text{eff}}(x)/r_0) - (\Delta\lambda/\lambda_{\text{res}})]^{1/2}$  is the WGM propagation constant,  $\beta_0 = 2\pi n_e/\lambda_{\text{res}}$  is the propagation constant in the bulk resonator material, and  $\Delta\lambda$  is the wavelength variation.

The theory described by Eqs. (1) and (2) has been previously applied to the design of different Surface Nanoscale Axial Photonics (SNAP) devices, e.g., miniature delay lines [19], buffers [20], and frequency comb generators [21]. Potential applications of this technology in the single photon regime require optimization of loss and coupling, which makes it critical to determine the dependencies of  $S_0(z)$ ,  $C(z)$ , and  $D(z)$ . This Letter reports the

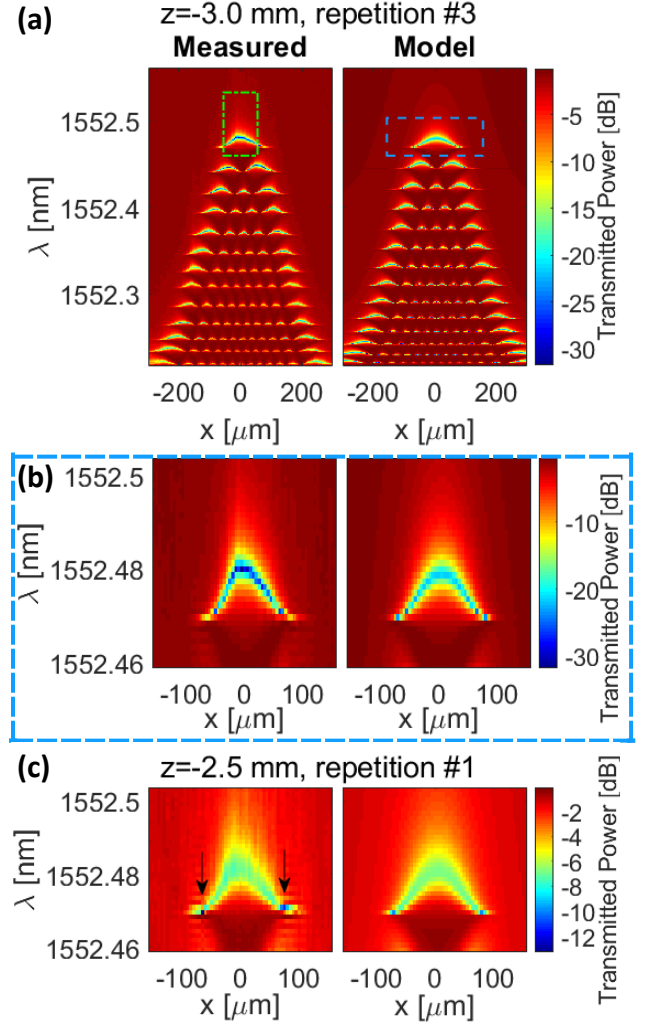


**Fig. 2.** (a) Comparison of measured and best-fit model spectrograms, near critical coupling, showing multiple axial modes. The green dot-dashed box over the measured data indicates the region used in coupling parameter fitting (see text). The blue dashed box over the model indicates the magnified region shown in (b) which compares the measured and best-fit model fundamental axial mode. (c) Comparison of measured and best-fit model fundamental resonances at  $z = -2.5 \text{mm}$  in the over-coupled regime. The characteristic edge dips seen in this regime are indicated with arrows on the measured data.

experimental characterization of these profiles along a tapered fiber, and the relationships between them.

Our experimental setup, illustrated in Fig. 1(b), consists of a  $\sim 400 \mu\text{m}$  long SNAP bottle resonator created on  $38 \mu\text{m}$  diameter fiber using a  $\text{CO}_2$  laser (see [22] and references therein), coupled to a microfiber pulled using a ceramic microheater [23]. Coupling parameters are estimated through the measurement and analysis of 2D spectrograms, e.g. Fig. 2(a) [22]. Spectrograms are made by combining the transmission spectrum through the microfiber at multiple contact positions  $x$  along the resonator with fixed  $z = \bar{z}$ . The transmission spectrum is calculated from the Jones matrix spectrum of the system, measured with a Luna Technologies

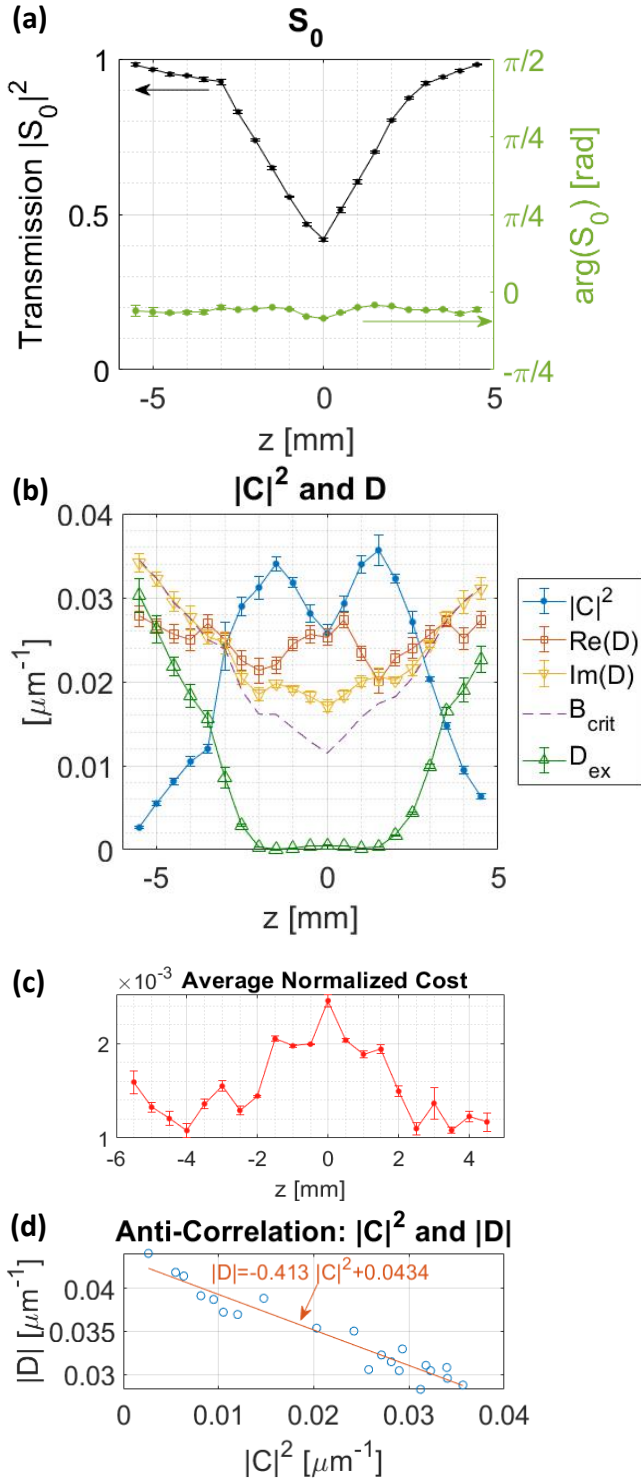


**Fig. 3.** Average coupling parameters with error bars showing standard deviation. (a) Nonresonant transmission power amplitude  $|S_0|^2$  with phase profile  $\arg(S_0)$ . (b)  $|C|^2$  and  $D$  parameters, with the critical coupling bound  $B_{\text{crit}}$  [Eq. (5)] and the excess resonant loss  $D_{\text{ex}}$  [Eq. (6)]. The profile of  $D_{\text{ex}}$  bears interesting similarity to the expected taper profile [23] (c) The average cost value normalized as described near Eq. (4), indicates excellent agreement between model and theory. (d) The average values of  $|C|^2$  and  $|D|$  display anti-correlation. The best-fit line approximately describes the interesting relationship where stronger coupling is associated with smaller effect on the cavity  $|D|$ .

Optical Vector Analyzer (OVA). We isolate the Jones matrix describing the taper segments past the microresonator from those describing the taper segments and connecting fibers using the procedure described in [24]. From this, we calculate our reported transmission values, which are for light with polarization matched to the resonator modes. The baseline taper loss (spectral average of 4.6 dB) is removed such that transmitted power fraction is 0 dB (no loss) in the absence of coupling.

We then fit the measured spectrogram data to extract the best-fit coupling parameters. To accomplish this, we first find the Green's function solution [15] to the 1D wave equation of Eq. (2). The effective radius variation serves as a potential of the assumed form

$$\Delta r_{\text{eff}}(x) = A \exp \left[ - \left( \frac{(x-x_0)^2}{2\sigma^2} \right)^p \right] + K. \quad (3)$$

We use a fitting procedure to find the values of  $A$ ,  $\sigma$ ,  $p$  and  $K$  that produce a modal eigenwavelength spectrum that best matches the observed spectrum. The best-fit values of  $A = 3.2744$  nm,  $\sigma = 123.5934$   $\mu\text{m}$ , and  $p = 1.1406$  are used for all resonators, while  $x_0$  and  $K$  are set for each spectrogram to account for the angle between the  $x$  and  $z$  axes being slightly different from  $90^\circ$ , and for random spectral shifts arising from thermal drift, respectively. Once the bare Green's functions  $G(\lambda, x, x)$ , for each spectrogram are found, the measured spectrograms are fit to Eq. (1) in the region indicated in the green box in Fig. 2(a) [see discussion below Eq. (5)] with fixed  $G(\lambda, x, x)$  to find the 5 best-fit real-valued local coupling parameters.

In some cases, the coupling parameter fits can converge to local minima that don't represent the actual coupling parameters. We determine when this occurs by comparing the best-fit model and experimental transmission amplitudes  $S_{11}(\lambda, x, z) = S_0(z) - \frac{i|C(z)|^2 G(\lambda, x, x)}{1 + D(z)G(\lambda, x, x)}$ . These two quantities are substantially different for local minima, and such a difference indicates that the fit needs to be run again with the local minima excluded, or with starting values closer to the true values. Local minima excluded, this procedure run on each spectrogram yields 5 real-valued coupling parameters,  $|S_0(z)|^2$ ,  $\arg[S_0(z)]$ ,  $|C(z)|^2$ ,  $\text{Re}[D(z)]$ , and  $\text{Im}[D(z)]$ , in addition to the final minimized "cost" value from the fit (described below). Each spectrogram measurement is repeated 4 times to assess repeatability, and the mean average values for these parameters and costs are plotted in Fig. 3 with the error bars showing the standard deviation of each quantity.

The interpretations of these parameters are as follows:  $|C|^2$  is the coupling strength, which peaks at  $z = \pm 1.5$  mm.  $|S_0|^2$  is the power transmission for light with nonresonant wavelength, with slope transitions at  $z = \pm 3$  mm and a minimum value near  $z = 0$  mm. The phase  $\arg(S_0)$  controls the shape of the resonances and is nearly flat across this range.  $D$  describes changes induced by the presence of the taper.  $\text{Re}(D)$  describes the shift of the resonance wavelength due to the presence of the taper and has a roughly flat profile with random variation [Fig. 3(a)], indicating that the phase shift experienced by WGMS passing the microfiber is roughly independent of the microfiber diameter. Finally,  $\text{Im}(D)$  describes broadening of the resonances due to excess loss induced by the presence of the microfiber.

The excellent agreement of our best-fit model and measured spectrograms is apparent from the low normalized cost [Fig. 3(c)]

$$\overline{\Delta P}(z) = \frac{\sqrt{\sum_{i,j} [P_{\text{meas}}(\lambda_i, x_j, z) - P_{\text{model}}(\lambda_i, x_j, z)]^2}}{HN}, \quad (4)$$

where  $P_{\text{meas}}$  and  $P_{\text{model}}$  are the measured and best-fit model transmission [Eq. (1)],  $i$  and  $j$  index grid positions, the numerator is the cost value, and the denominator normalizes the cost by  $N$ , the number of transmission values in the fit region [green box in Fig. 2(a); the model has the same number of transmission values as the measured spectrograms], and  $H$ , the depth of the measured fundamental axial resonance along its central position ( $x=0$ ). This quantifies the fractional variation per measured transmission value. The effectiveness of the local approach is validated by the small value of  $\Delta\bar{P}(z)$  across the entire profile.

Starting from the Fano formulation of transmission [Eq. (13) of [15]], and neglecting intrinsic material loss, it can be shown that the coupling parameters determine the coupling regime. Critical coupling occurs when  $|C(z)|^2$  equals the criticality bound

$$B_{\text{crit}}(z) = \frac{|S_0(z)|^2 \text{Im}[D(z)]}{\text{Re}[S_0(z)]}. \quad (5)$$

The resonator-taper system is in the over-coupled regime when  $|C(z)|^2 > B_{\text{crit}}(z)$ , and in the undercoupled regime when  $|C(z)|^2 < B_{\text{crit}}(z)$ . This relationship also implies that the local group delay of individual axial modes is positive (negative) in the over-coupled (undercoupled) regime, c.f. Eq. (8) of [25].

Where  $|z| > 3.0$  mm in Fig. 3(b), the system is undercoupled and  $B_{\text{crit}}(z) \approx \text{Im}[D(z)]$ . At  $z = \pm 3.0$  mm, the power transmission for resonant light is very small (<2%; even deeper in Fig. 2). This and the nearby crossings of  $B_{\text{crit}}(z)$  and  $|C(z)|^2$  both indicate that coupling is close to critical at these positions. Between these critical coupling positions, the system is over-coupled and it's important to perform the check described above against local minima. The transmission is very sensitive to small changes in over-coupled and critically-coupled configurations, and since our system uses no feedback stabilization, we note a concomitant increase in the standard deviation of  $|C|^2$  in those regimes. We observe that the dips near the edges of the resonances in spectrograms [Fig. 2(c)] are indicative of over-coupling. The increased variation in these dips can confound the fit, which is why we select the fit-region indicated in Fig. 2(a).

The coupling parameters indicate device loss performance. Energy conservation sets two constraints on the coupling parameters [15]:

$$|S_0(z)| \leq 1 \quad \text{AND} \quad \text{Im}[D(z)] > |C(z)|^2 \frac{1 - \text{Re}[S_0(z)]}{1 - |S_0(z)|^2}, \quad (6)$$

which set bounds on the nonresonant and resonant loss, respectively. Minimum loss occurs when each of these conditions approaches equality. We quantify how much  $\text{Im}[D(z)]$  exceeds this minimum with the excess resonant loss

$$D_{\text{ex}}(z) = \text{Im}[D(z)] - |C(z)|^2 \frac{1 - \text{Re}[S_0(z)]}{1 - |S_0(z)|^2}, \quad (7)$$

and note the interesting qualitative similarity of its profile to the expected shape of our microfiber taper from the model in [23] [Fig. 3(b)]. Investigation of the suggested proportionality relationship between the excess loss and the local radius of the microfiber at the point of contact is an interesting avenue for future research that could potentially be used to determine the microfiber radius variation (see e.g. [26]). We find a strong anti-correlation relationship between  $|C|^2$  and  $|D|$  (correlation coefficient = -0.96) [Fig. 3(d)], which indicates that the taper's effect on the cavity field (through resonant frequency shifts and induced loss) is smallest where the coupling is largest.

In conclusion, we report experimental characterization of the local coupling parameters, which describe the interaction between an elongated bottle microresonator and an input-output microfiber. In contrast to parameters commonly used for the description of the microresonator-waveguide coupling, these parameters are independent of the mode distribution. Our fitting approach demonstrates excellent agreement between measured and best-fit theoretical models, in addition to good coupling parameter repeatability between consecutive spectrogram measurements, in all coupling regimes (undercoupled through over-coupled). This method of characterizing coupling and loss paves the way for design optimization towards classical and quantum resonant optical devices. The elongated shape of the modes is of special importance since it allows us to simplify positioning of quantum emitters [27]. We suggest that, for this purpose, the microresonator profile can be optimized to arrive at enhanced regions with uniform WGM magnitude.

**Funding.** US Army Research Laboratory Fellowship Program (W911NF-19-2-0103); Engineering and Physical Sciences Research Council (EP/P006183/1).

**Disclosures.** The authors declare no conflicts of interest.

## References

- [1] K. J. Vahala, *Nature* **424**, 839 (2003).
- [2] A. B. Matsko, *Practical Applications of Microresonators in Optics and Photonics* (Boca Raton, FL, CRC Press, 2009).
- [3] G. C. Righini, et al., *Riv Nuovo Cimento* **34**, 43 (2011).
- [4] B. E. Little, J.-P. Laine, and H. A. Haus, *J. Lightwave Technol.* **17**, 704 (1999).
- [5] M. L. Gorodetsky and V. S. Ilchenko, *J. Opt. Soc. Am. B* **16**, 147 (1999).
- [6] M. Cai, O. Painter, and K. J. Vahala, *Phys. Rev. Lett.* **85**, 74 (2000).
- [7] S.M. Spillane, et al., *Phys. Rev. Lett.* **91**, 043902 (2003).
- [8] M. J. Humphrey, E. Dale, A.T. Rosenberger, and D.K. Bandy, *Optics Commun.* **271**, 124 (2007).
- [9] C.-L. Zou, et al., *J. Opt. Soc. Am. B* **25**, 1895 (2008).
- [10] A. Chiasera et al., *Laser Photon. Rev.* **4**, 457 (2010).
- [11] S. B. Gorajooobi, G. S. Murugan, and M. N. Zervas, *Opt. Express* **26**, 26339 (2018).
- [12] H. J. Kimble, *Nature* **453**, 1023 (2008).
- [13] J. Volz, M. Scheucher, C. Junge and A. Rauschenbeutel, *Nat. Photon.* **8**, 965 (2014).
- [14] A. Reiserer and G. Rempe "Cavity-based quantum networks with single atoms and optical photons," *Rev. Mod. Phys.* **87**, 1379 (2015).
- [15] M. Sumetsky, *Opt. Express* **20**, 22537 (2012).
- [16] L. Tong, J. Lou, and E. Mazur, *Opt. Express* **12**, 1025 (2004).
- [17] T. Tsuchizawa et al., *IEEE J. Sel. Top. Quantum Electron.* **11**, 232 (2005).
- [18] M. Sumetsky and J. Fini, *Opt. Express* **19**, 26470 (2011).
- [19] M. Sumetsky, *Phys. Rev. Lett.* **111**, 163901 (2013).
- [20] M. Sumetsky, *Sci. Rep.* **5**, 18569 (2015).
- [21] S. V. Suchkov, M. Sumetsky, and A. A. Sukhorukov, *Opt. Lett.* **42**, 2149 (2017).
- [22] M. Sumetsky, *Nanophotonics* **2**, 393 (2013).
- [23] L. Ding, C. Belacel, S. Ducci, G. Leo and I. Favero, *Appl. Opt.* **49**, 2441 (2010).
- [24] M. Crespo-Ballesteros, Y. Yang, N. Toropov, and M. Sumetsky, *Opt. Lett.* **44**, 3498 (2019).
- [25] M. Sumetsky, *Opt. Express* **21**, 15268 (2013).
- [26] M. Sumetsky et al., *Opt. Lett.* **31**, 2393 (2006).
- [27] Y. Colombe, T. Steinmetz, G. Dubois, F. Linke, D. Hunger, and J. Reichel, *Nature* **450**, 272 (2007).